Nano Research

Open Access

Research Article

Boosting charge extraction and efficiency of inverted perovskite solar cells through coordinating group modification at the buffer layer/cathode interface

Zhiqing Liang[1,§], Ziqiu Ren[1,§], Ziyu Wang[1]✉, Nan Yan[2], Ling Li[1], Bo Zhang[1], and Yanlin Song[3]✉

[1] College of Chemistry, Zhengzhou University, Zhengzhou 450052, China
[2] Key Laboratory of Applied Surface and Colloid Chemistry Ministry of Education, Shaanxi Key Laboratory for Advanced Energy Devices, Shaanxi Engineering Lab for Advanced Energy Technology School of Materials Science and Engineering, Shaanxi Normal University, Xi'an 710119, China
[3] Key Laboratory of Green Printing, Institute of Chemistry, Chinese Academy of Sciences (ICCAS), Beijing Engineering Research Center of Nanomaterials for Green Printing Technology, National Laboratory for Molecular Sciences (BNLMS), Beijing 100190, China
§ Zhiqing Liang and Ziqiu Ren contributed equally to this work.

Cite this article: *Nano Research*, **2025**, *18*, 94907075. https://doi.org/10.26599/NR.2025.94907075

ABSTRACT: In inverted perovskite solar cells (PSCs), effective modification of the interface between the metal cathode and electron transport layer (ETL) is crucial for achieving high performance and stability. Herein, sulfonated bathocuproine, commonly known as disodium bathocuproine disulfonate (BCDS), was employed as a cathode buffer layer to address the interfacial issues at the [6,6]-phenyl-C61-butyric acid methyl ester (PCBM)/Ag interface. BCDS possesses the ability to form coordinate bonds with Ag electrodes. The utilization of the BCDS buffer layer enhanced the charge extraction capability at the cathode interface while simultaneously achieving interfacial defect passivation, improving interfacial contact and increasing the built-in electric field. Consequently, a power conversion efficiency (PCE) of 25.06% was achieved. Furthermore, owing to the excellent film-forming uniformity of BCDS on PCBM, the stability of the device was also improved. After storage in dry air for more than 2000 h, the device maintained 96% of its initial efficiency. This work underscores the remarkable potential of tailoring coordination groups to enhance charge extraction efficiency at the ETL–cathode interface, unveiling a promising new frontier in buffer layer development and performance optimization strategies for PSCs.

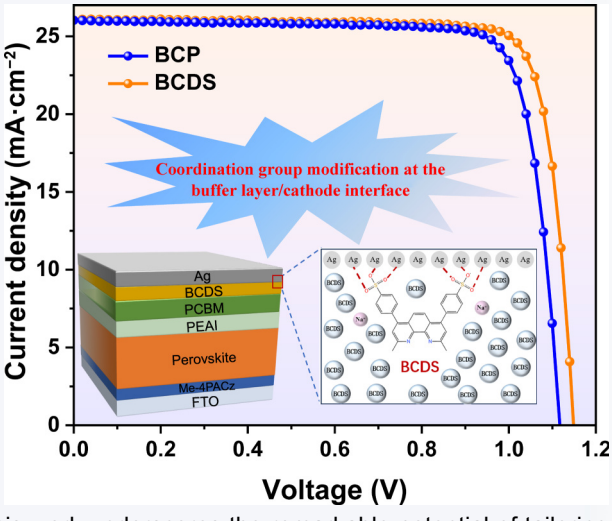

KEYWORDS: perovskite solar cells, buffer layer, bathocuproine disulfonate, coordination group modification, electron transport layer (ETL)–cathode interface

1 Introduction

Perovskite solar cells (PSCs) have attracted significant attention because of their exceptional carrier mobility, prolonged carrier lifetime, high light-absorption coefficient, minimal exciton binding energy, outstanding defect tolerance and adjustable bandgap [1, 2]. Over the past decade, PSCs have exhibited remarkable progress in power conversion efficiency (PCE), with laboratory-certified PCE surpassing 26.1% [3, 4], which is comparable to that of state-of-the-art crystalline silicon solar cells. PSCs can be categorized into two primary device structures: normal (n–i–p) and inverted (p–i–n). Compared to conventional devices, inverted-structure devices offer advantages such as simplified fabrication processes, low-temperature deposition techniques, the absence of hysteresis effects and compatibility with tandem configurations involving traditional solar cells, such as silicon-based and copper indium gallium

Received: August 14, 2024; **Revised:** September 30, 2024
Accepted: October 14, 2024

✉Address correspondence to Ziyu Wang, zywang@zzu.edu.cn; Yanlin Song, ylsong@iccas.ac.cn

selenide (CIGS) based solar cells [5, 6]. However, early stage inverted perovskite solar cells exhibited lower open-circuit voltages (V_{oc}) owing to limitations in hole transport layer (HTL) materials, resulting in a lower PCE than that of conventional devices [7, 8]. Recently, phosphonic acid group-anchored carbazole-based self-assembled monolayers (SAMs) have emerged as an effective solution to this issue in inverted perovskite solar cells [9, 10]. By reducing the defect density at the interface and suppressing nonradiative recombination, SAMs significantly enhance the V_{oc} and fill factor (FF) of the device, thereby enabling inverted PSCs to gradually surpass their conventional counterparts in terms of efficiency [11]. This highlights the unique efficacy of interface engineering in enhancing device performance.

High-performance inverted PSCs encounter challenges in the electron transport layer (ETL). Fullerene and its derivative [6,6]-phenyl-C_{61}-butyric acid methyl ester (PCBM) have been extensively employed as electron transport materials in inverted PSCs. PCBM effectively passivates the trap states of the perovskite films and facilitates efficient electron transport, reducing the hysteresis in inverted PSCs [12, 13]. However, when PCBM interfaces with metals having a high work function, charges tend to diffuse into the metal, creating an upward-curved interface energy level and a Schottky barrier, which severely restricts the extraction of electrons by the metal electrode [14, 15]. Additionally, the limited solubility and low viscosity of PCBM solutions often lead to the formation of pinholes, which facilitate direct contact between the perovskite and metal electrode, thereby promoting charge recombination at the interface [16]. Consequently, devices employing pure PCBM as the ETL often exhibit suboptimal performance [15, 17]. The introduction of a cathode buffer layer between the PCBM and the metal electrode is an effective approach for addressing cathode interface issues [18]. The incorporation of an ideal buffer layer facilitates directional electron flow from PCBM to the metal electrode, enhancing charge extraction and reducing charge recombination. This ultimately improves the device performance and stability [19, 20]. Accordingly, several studies have utilized various cathode buffer layers, including thermally evaporated Ca [21], Bi [22], LiF [23] and 1,3,5-tris(1-phenyl-1H-benzimidazol-2-yl)benzene (TPBI) [24], oxide metal deposited by atomic layer deposition (e.g., ZnO [25], TiO_2 [26] and SnO_2 [14, 27]) and rhodamine derivatives [28]. Among these alternatives, bathocuproine (BCP) is commonly employed because of its deep valence band (VB), which effectively blocks hole carriers and ease of preparation via solution-based film spinning methods [29, 30]. However, the poor electrical conductivity of BCP reduces the charge transfer efficiency between the perovskite and the cathode, leading to suboptimal device performance. To address this issue, Yang et al. doped BCP with 1,3,5-triazine-2,4,6-trithiol trisodium salt (TTTS) to enhance its conductivity and coordination ability with an Au electrode, thereby improving its electron transport capacity and device efficiency [31]. Their study demonstrates an effective modification method for BCP buffer layers. Chemical modification of metal electrodes can regulate their electrochemical properties and enhance charge extraction capability. Chen et al. achieved this by modifying the inner surface of Cu electrodes using mercaptopyridine-based molecules, allowing fine-tuning of the electronic and chemical properties via substituent modifications of mercaptopyridines [32]. Consequently, they successfully manipulated the Fermi level of the Cu electrodes and improved the interfacial charge extraction.

In this study, we introduce disodium bathocuproine disulfonate (BCDS) as an innovative alternative to BCP in inverted PSCs, serving as a buffer layer that bridges the PCBM and the Ag electrode. BCDS is a sulfonated derivative of BCP, with two sulfonic acid groups introduced into the BCP molecule, each capable of coordinating with metals through three oxygen atoms. This enhanced the chemical coordination between the sulfonate group and the Ag electrode, facilitating efficient electron extraction from the perovskite to the electrode. Additionally, BCDS exhibited superior conductivity compared to BCP, leading to improved charge extraction efficiency. Moreover, band alignment in BCDS exhibited excellent compatibility. Furthermore, the BCDS layer formed a dense structure on top of the PCBM film, effectively passivating the surface of the perovskite film and preventing direct contact between the perovskite layer and the electrode through pinholes in the PCBM film. Consequently, PSCs incorporating BCDS as the cathode buffer layer achieved an impressive PCE of 25.06%. The use of coordination groups to increase charge extraction efficiency at the buffer layer–cathode interface offers a groundbreaking approach for future advancements in buffer layer.1.

2 Experimental

2.1 Materials

The patterned fluorine-doped tin oxide (FTO) substrates, lead iodide (PbI_2, 99.999%), formamidinium (FA) iodide (FAI, 99.5%), methylamine (MA) hydrochloride (MACl, 99.5%), cesium iodide (CsI, 99.999), phenethylammonium iodide (PEAI, 99.9%), lead bromide ($PbBr_2$, 99.99%), methylammonium bromide (MABr, 99.9%), PCBM (99.9%), [4-(3,6-dimethyl-9H-carbazol-9-yl)butyl]phosphonic acid (Me-4PACz, 99%) and bathocuproine (BCP, > 99.0%) were purchased from Advanced Election Technology Co., Ltd. (China). Disodium BCDS (97%), ethyl acetate (EA, 99.9%), chlorobenzene (CB, 99.9%), isopropyl alcohol (IPA, 99.5%), N,N-dimethylformamide (DMF, 99.5%) and dimethyl sulfoxide (DMSO, 99.9%) were purchased from Alfa Aesar (USA).

2.2 Device fabrication

FTO glass substrates were sequentially ultrasonicated with detergent, deionized water, acetone and isopropanol. Next, they were dried using an N_2 flow and then treated with ultraviolet (UV) ozone for 15 min. The substrates were immediately transferred to a N_2-filled glovebox. Me-4PACz solution (0.5 mg·mL^{-1} in IPA) was spin-coated onto the substrate at 3000 rpm for 30 s followed by annealing on a hot plate at 100 °C for 10 min. The 1.5 M perovskite precursor solution with a composition of $Cs_{0.05}(FA_{0.98}MA_{0.02})_{0.95}Pb(I_{0.99}Br_{0.01})_3$ with 5 mol% excess PbI_2 and 10 mol% MACl additive was prepared by dissolving CsI, FAI, PbI_2, MABr, $PbBr_2$ and MACl in a molar ratio of 0.05:0.93:1.04:0.02:0.01:0.10 in a mixed solvent of DMF and DMSO with a volume ratio of 4:1. The precursor solution was spin coated onto the FTO/Me-4PACz substrate at 1000 rpm for 10 s. Then, it was rotated at 4000 rpm for 40 s. During this step, 150 μL EA was dropped on the substrate as the anti-solvent at 15 s before the end of the process. The perovskite film (650 nm) was obtained by annealing at 100 °C for 30 min. Subsequently, PEAI (1 mg·mL^{-1} in IPA) was deposited on the perovskite film at 4000 rpm for 30 s. This was followed by annealing the film at 100 °C for 5 min. Subsequently, the PCBM

solution (20 mg·mL^{-1} in CB) was spin-coated onto the perovskite film at 4000 rpm for 30 s to obtain a PCBM layer (60 nm). The BCDS or BCP (0.5 mg·mL^{-1} in IPA) solution was then spin coated onto the PCBM film samples at 4000 rpm for 30 s to obtain 10 nm-thick buffer layers. Finally, 100 nm of Ag was deposited as an electrode by thermal evaporationusing a shadow mask (0.04 cm^2).

2.3 Characterization

Current density–voltage (*J*–*V*) tests were conducted under simulated solar illumination (AM 1.5G, 1 sun) using a B2901A source meter equipped with a solar simulator (Enlitech, SS-X50, Taiwan, China). The photoluminescence (PL) and time-resolved PL (TRPL) spectra were obtained using a fluorescence spectrometer (HORIBA FluoroMax, Japan). The external quantum efficiency (EQE) of the devices were measured using a quantum-efficiency-measuring instrument (QE-R, Enlitech, Taiwan, China). The transient photocurrent (TPC), transient photovoltage (TPV) and space charge-limited current (SCLC) of the solar cells were measured using a solar cell carrier characteristics analyzer (PAIOS, Fluxim, Switzerland). UV–vis absorption spectra were obtained using a Cary 5000 spectrophotometer (Agilent Technologies, USA). Furthermore, scanning electron microscopy (SEM) images were acquired using a Regulus 8100 microscope (Hitachi, Japan). Moreover, X-ray photoelectron spectroscopy (XPS) and ultraviolet photoelectron spectroscopy (UPS) were conducted using a K-Alpha (Thermo Scientific, USA) and Escalab Xi+ spectrometers (Thermo Scientific, USA), respectively.

3 Results and discussion

3.1 Device structure and photovoltaic performance

The inverted PSCs were structured as FTO/Me-4PACz/perovskite/PCBM/BCDS/Ag, where Me-4PACz represents [4-(3,6-dimethyl-9H-carbazol-9-yl)butyl]phosphonic acid and FTO represents fluorine-doped tin oxide, as illustrated in Fig. 1(a). Furthermore, as shown in Fig. 1(b), the molecular structure of BCDS enables its coordination with the Ag electrode via the oxygen atoms in its sulfonic acid group on the benzene ring. This coordination reinforces the bond between the Ag electrode and the buffer layer, thereby enhancing the efficiency of the photogenerated electron transfer to the Ag electrode. A cross-sectional SEM image of the proposed BCDS-based device is shown in Fig. S1 in the Electronic Supplementary Material (ESM). To evaluate the impact of BCDS as a cathode buffer layer in operational PSCs, we measured the *J*–*V* curves of the PSCs without a buffer layer and of those with BCP and BCDS buffer layers. The results are shown in Figs. 1(c) and 1(d) and Fig. S2 in the ESM. Devices without a buffer layer, referred to as pure PCBM, exhibited the lowest performance, achieving a PCE of only 19.32%. This inferiority stems from the Schottky barrier formed between the PCBM and the metal electrode, which impedes electron transport to the electrode [33]. After introducing a buffer layer between the PCBM and the metal electrode, the efficiency significantly improved. Specifically, the BCDS-based devices greatly outperformed their BCP-based counterparts, with the PCE increasing from 23.35% to 25.06%. This improvement is primarily attributed to an increase in V_{oc} from 1.106 to 1.147 V, an increase in short-circuit current density (J_{sc}) from 25.86 to 26.05 mA·cm^{-2} and that in the FF from 81.68% to 83.87% when operated in the reverse direction. The statistical distributions of V_{oc}, J_{sc}, FF and PCE were determined by analyzing 20 individual cells of different devices (Fig. S3 in the ESM). The photovoltaic parameters are listed in Tables S1–S3 in the ESM. Compared with the BCP-based devices, the BCDS-based devices demonstrated significantly higher V_{oc}, J_{sc} and FF with a narrower data distribution, indicating enhanced repeatability.

The incident photon-to-electron conversion efficiency (IPCE) of the PSCs was measured as shown in Fig. 1(e). Compared with the BCP-based device, the BCDS-based device exhibited a slightly higher IPCE across the entire wavelength region. The integrated J_{sc} values of devices based on BCP and BCDS were in accordance with their respective *J*–*V* curves, measuring approximately 25.11 and

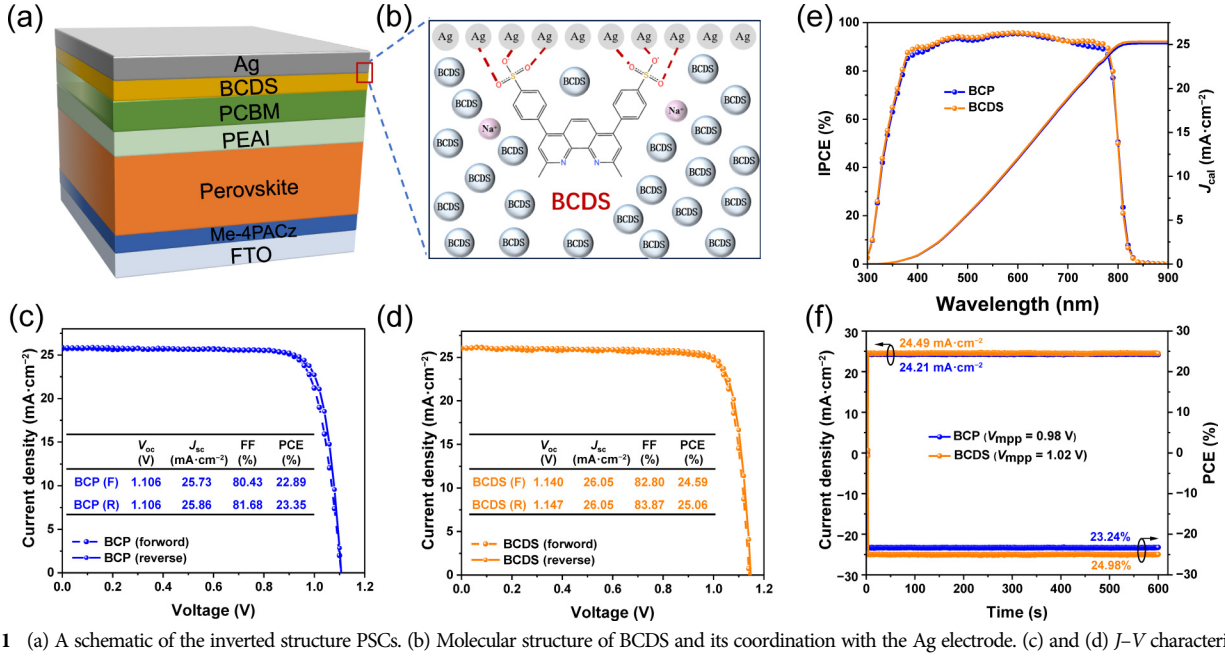

Figure 1 (a) A schematic of the inverted structure PSCs. (b) Molecular structure of BCDS and its coordination with the Ag electrode. (c) and (d) *J*–*V* characteristics of the superior BCP-based and BCDS-based device. (e) IPCE values of PSCs and their corresponding integrated J_{sc} values. (f) Photocurrents and PCEs versus time of the PSCs based on BCP and BCDS biased at their maximum power point voltages of 0.96 and 1.02 V, respectively.

25.35 mA·cm^{-2}, respectively. In addition, the steady-state photocurrent and stabilized power output (SPO) were evaluated at the maximum power point (0.96 and 1.02 V for the BCP- and BCDS-based devices, respectively), as illustrated in Fig. 1(f). The SPO values of the BCP- and BCDS-based devices reached 23.24% and 24.98%, respectively, aligning well with their corresponding *J*–*V* curves. For comparison, the SPO value of the pure PCBM device rapidly decreased from 18.4% to 15.6% within the first 50 s, which can be attributed to the poor contact between PCBM and the Ag electrode (Fig. S4 in the ESM). Moreover, we fabricated scaled-up devices with an active area of 1 cm^2, as illustrated in Fig. S5 in the ESM. The 1 cm^2 BCDS-based device afforded an impressive PCE of 22.76% with the 1.142 V of V_{oc}, 25.64 mA·cm^{-2} of J_{sc} and 77.70% of FF. Those parameters surpassed those of the BCP-based counterpart, which demonstrated a PCE of 19.36%, V_{oc} of 1.082 V, J_{sc} of 25.17 and FF of 71.11%. This result indicates that the strategy of replacing BCP with BCDS is feasible for large-area devices.

The long-term stabilities of the devices were assessed, as shown in Fig. S6 in the ESM. The unencapsulated devices were stored in dry air at 25 °C for over 2000 h. During this period, the BCDS-based device maintained 96% of its initial efficiency, representing a slight improvement over the BCP-based device, which retained 93% of its initial efficiency. Considering that solar cells operate under illumination, the light stability of the devices was also evaluated, as depicted in Fig. S7 in the ESM. Following 480 h of exposure to 1 sun simulated solar light in the glove box, the BCDS-based device exhibited remarkable stability, retaining 90% of its initial efficiency, whereas the BCP-based device maintained 81% of its initial performance. These results demonstrate the superior performance of BCDS as a cathode buffer layer in inverted PSCs.

3.2 Characterization of BCDS film

The electrical conductivities of the BCDS and BCP films were determined by conducting *J*–*V* measurements on devices with indium tin oxide (ITO)/BCDS (or BCP)/Ag structures, as shown in Fig. 2(a). The conductivity of the BCDS film was measured to be 2.68 × 10^{-6} S·cm^{-1}, which is higher than that of the BCP film, which yielded a conductivity of 2.17 × 10^{-6} S·cm^{-1}. The enhanced conductivity of the BCDS film can augment its electron transport capability, thereby improving the overall device performance. Figure 2(b) shows the UV–vis absorption spectra of the BCP and BCDS films. As shown, light absorption in the visible region observed for the BCDS film was significantly lower compared to that achieved by the BCP film. This finding holds great significance for the currently popular bifacial solar cells, as a portion of the incident light penetrates the perovskite absorption layer from the buffer layer side and the weak absorption of BCDS helps minimize the parasitic absorption within the device [34].

The Fermi levels (E_F) of BCP and BCDS were measured using UPS and the results are shown in Fig. 2(c). E_F can be calculated using the equation $E_F = E_{cut} - 21.22$ eV, where E_{cut} represents the cut-off binding energy and 21.22 eV corresponds to the emission energy of helium irradiation. The E_{cut} value of BCP was 16.98 eV, whereas that of BCDS was slightly higher at 16.99 eV. Thus, the calculated E_F values for BCP and BCDS were −4.24 and −4.23 eV, respectively. Moreover, the Fermi edge (E_{edge}) values for BCP and BCDS were determined to be 2.86 and 2.81 eV, respectively. The valence band maximum (E_{VB}) can be calculated using the equation $E_{VB} = E_F - E_{edge}$, resulting in E_{VB} values of −7.10 and −7.04 eV for BCP and BCDS, respectively. Based on the tauc plot derived from absorption spectra (Fig. S8 in the ESM), the bandgap energy (E_g)

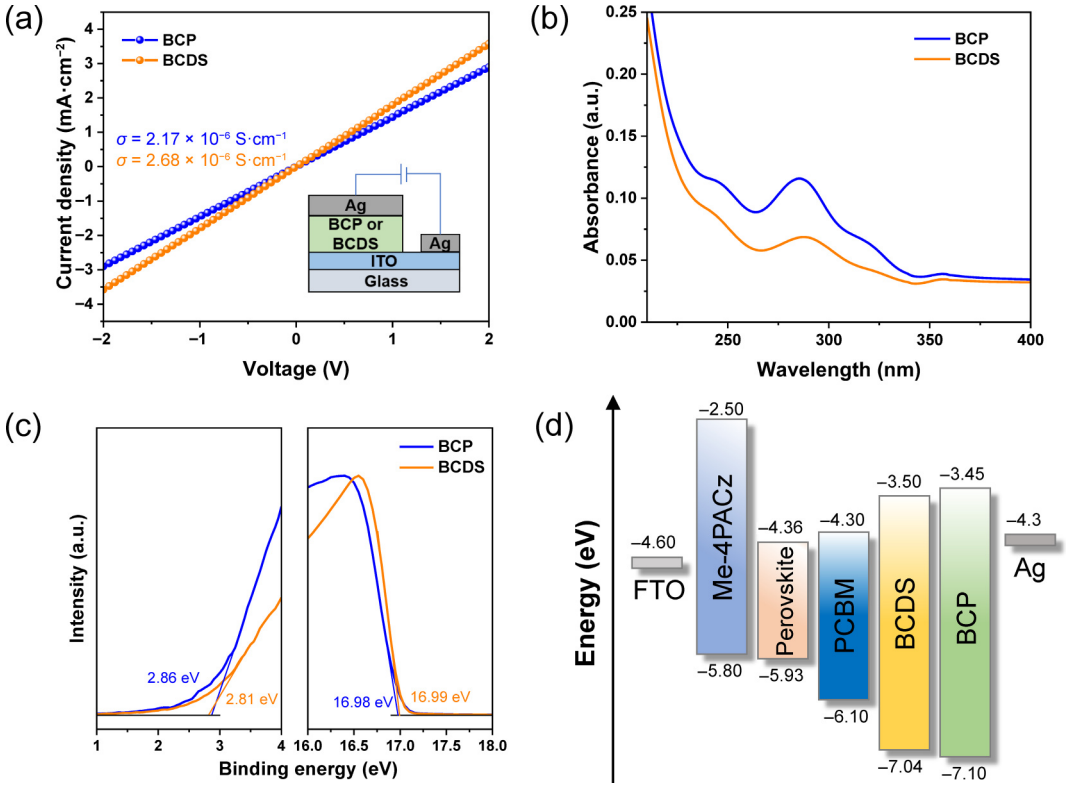

Figure 2 (a) Conductivity measurements of BCDS and BCP films. The inset figure shows the device structure with ITO/BCP (or BCDS)/Ag design. The BCDS and BCP layers have the same thickness of 10 nm. (b) UV–vis absorbance spectra. (c) UPS spectra. (d) Energy level diagram of the BCDS and BCP films relative to those of other layers in the perovskite device.

values of 3.65 and 3.54 eV were obtained for BCP and BCDS, respectively. The corresponding conduction band (E_{CB}) values were calculated according to the equation $E_{CB} = E_g + E_{VB}$ as −3.50 and −3.45 eV for BCP and BCDS, respectively. Figure 2(d) shows the energy-level diagrams of BCP and BCDS in the perovskite devices. The corresponding data are detailed in Table S4 in the ESM. In comparison with BCP, BCDS exhibited a comparable Fermi level, yet it demonstrated a shift in E_{CB} to a deeper level by 0.05 eV. This observation suggests that BCDS has a higher electron affinity and a narrower energy gap between PCBM and the buffer layer, thereby indicating a reduced barrier for electron transport and enhanced electron extraction capability [31].

3.3 Interaction between BCDS and Ag electrode

The interaction between BCDS and the Ag electrode was investigated using Fourier-transform infrared spectroscopy (FTIR) (Fig. 3(a)) and XPS (Figs. 3(b) and 3(c)). The FTIR tests were conducted by thermally evaporating Ag onto the BCDS film, scraping off the powder and laminating it with potassium bromide (KBr). On the other hand, the XPS tests were performed by thermally evaporating an 8 nm Ag film on the BCP and BCDS films. The BCDS films exhibited bands at 1128.3 and 1222–1195 cm^{-1}, which can be attributed to the symmetric (ν_{as} S=O) and asymmetric (ν_{as} S=O) stretching of the sulfonate group [35–37]. These bands were red-shifted to lower wavenumbers after the deposition of Ag, indicating a potential interaction between the sulfonate group and Ag. This hypothesis was further supported by XPS testing. The binding energies of the two 3d peaks of Ag deposited on BCP were observed at 373.92 and 367.92 eV, respectively, while those deposited on BCDS exhibited a shift towards higher binding energy (374.13 eV, 368.13 eV). Considering that the sole distinction between BCDS and BCP is the presence of sulfonate groups, it can be inferred that these groups exhibited a strong interaction with the Ag electrode. The deconvolution analysis of O 1s spectra reveals two distinct peaks corresponding to BCDS at 531.44 and 529.74 eV. The first peak at 531.44 eV was attributed to the oxygen atoms originating from the sulfonate groups, while the second peak at 529.74 eV was assigned to the S=O bonds within the sulfonate groups [38]. However, upon deposition of an 8 nm Ag layer on the BCDS film, a blue shift in the O 1s spectrum was observed with peak values at approximately 532.33 and 530.63 eV and the content of S=O decreased significantly. This suggests that certain S=O groups underwent transformation into S–O bonds owing to the coordination between the sulfonate group and Ag, as shown in Fig. 1(b). The strong interaction between BCDS and Ag facilitated the conformal deposition of the Ag electrode, thereby promoting efficient electron extraction from the ETL to the Ag electrode.

To investigate the buried surface of the Ag electrodes on the BCP and BCDS films, we deposited 20 nm Ag films onto the BCP and BCDS films and conducted SEM and atomic force microscopy (AFM) imaging, as shown in Fig. 4. As evidenced by the SEM and AFM tests, both the BCP and BCDS films exhibited uniform morphologies (Figs. 4(a) and 4(b)). However, the BCDS film possessed more microstructures, leading to a slightly higher surface roughness than that of the BCP film (Figs. 4(e) and 4(f)). Following the deposition of a 20 nm Ag film, the Ag film on the BCDS displayed a denser and more uniform morphology (Figs. 4(c) and 4(d)). According to the surface roughness data obtained from the AFM tests, while the BCP film originally had a roughness of 4.22 nm, the roughness increased to 4.82 nm after the deposition of 20 nm of Ag. Conversely, despite the BCDS film initially exhibiting

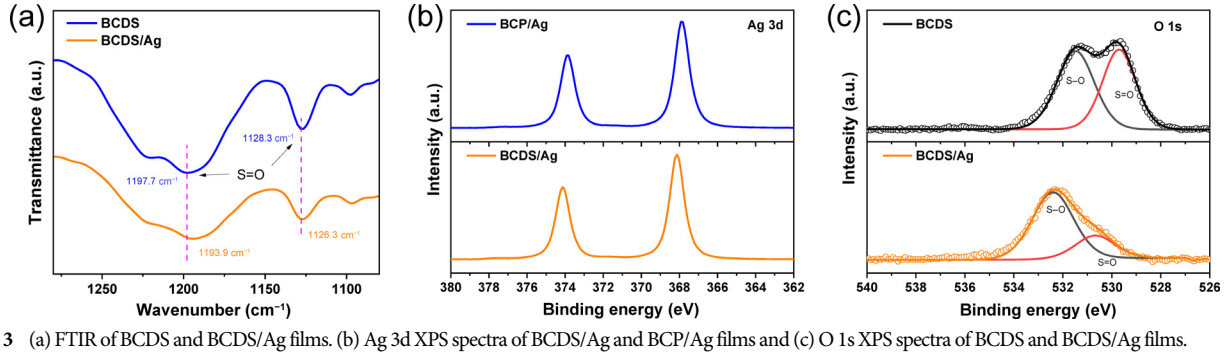

Figure 3 (a) FTIR of BCDS and BCDS/Ag films. (b) Ag 3d XPS spectra of BCDS/Ag and BCP/Ag films and (c) O 1s XPS spectra of BCDS and BCDS/Ag films.

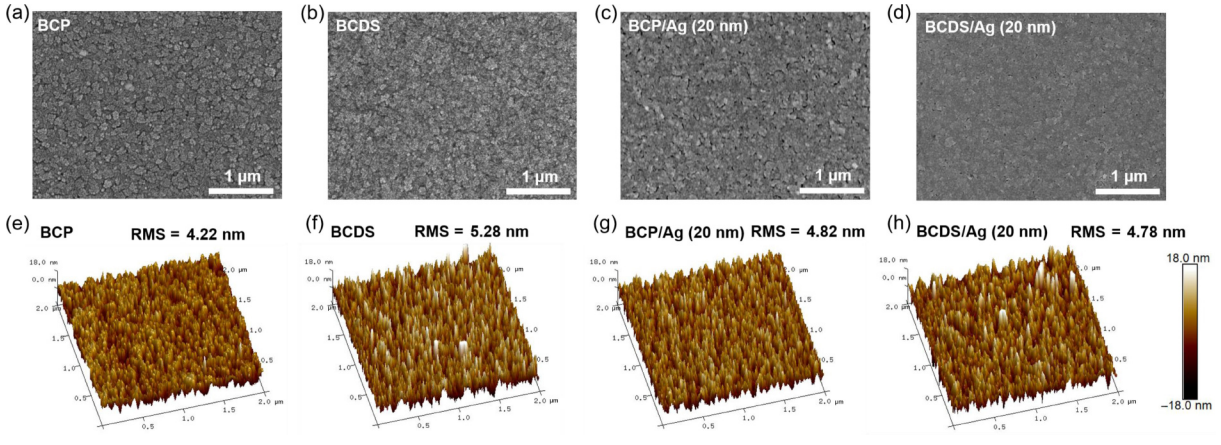

Figure 4 SEM images of (a) BCP, (b) BCDS, (c) BCP/Ag (20 nm), and (d) BCDS/Ag (20 nm) films coated on ITO substrates. AFM images of (e) BCP, (f) BCDS, (g) BCP/Ag (20 nm), and (h) BCDS/Ag (20 nm) films coated on ITO substrates.

a roughness of 5.28 nm, the roughness decreased to 4.78 nm after depositing 20 nm Ag. This contrasting result further supports the presence of a strong chemical interaction between BCDS and Ag, which promotes the conformal growth of the Ag film [39].

3.4 Carrier extraction and recombination in devices

To comprehensively examine the influence of the BCDS buffer layer on the charge-extraction capability of the Ag cathode, we fabricated half-devices with a glass/perovskite/PCBM/BCDS (or BCP)/Ag structure. Steady-state PL (Fig. 5(a)) and TRPL (Fig. S9 in the ESM) spectroscopies were conducted to analyze the charge-extraction process within these half-devices. Notably, for the optimized PL analysis, the thickness of the Ag layer was precisely controlled to 8 nm via thermal deposition and the laser beam was incident from the Ag electrode side. The fitting parameters of TRPL are detailed in Table S5 in the ESM. Compared with the BCP half device, the BCDS half device exhibited higher fluorescence quenching and reduced carrier lifetime, with 1.30 ns for BCDS and 1.42 ns for BCP, respectively. In addition to the higher conductivity of BCDS relative to BCP, the coordination interaction between BCDS and Ag enhanced the ability of the electrode to extract photogenerated electrons from the perovskite films. We conducted *J*–*V* curve measurements on BCP and BCDS devices in the dark (Fig. S10 in the ESM). Lower leakage current was observed in the BCDS device, suggesting a more efficient electron extraction, which minimizes recombination. These findings are in accordance with the PL and TRPL results. TPV and TPC tests were performed to further assess the carrier dynamics within the device. The results indicated that the BCDS-based device displayed a slower photovoltage decay (Fig. 5(b)) and faster photocurrent decay (Fig. S11 in the ESM), indicating reduced carrier recombination and an enhanced charge extraction rate [40].

The trap-related charge recombination in the devices was investigated by measuring the *J*–*V* characteristics under varying light intensities (P_{light}). Figure S12 in the ESM plots the measured J_{sc} as a function of light intensity. The relationship between J_{sc} and P_{light} can be described by the formula $J_{sc} \propto P^S$, where $S = 1$ signifies complete extraction and collection of all free carriers on the electrode before their recombination, while $S < 1$ indicates some degree of bimolecular recombination. The BCP-based device exhibited an S value of 0.973, which is slightly lower than 1, whereas the BCDS-based device demonstrated an S value of 0.997. This result suggests that BCDS enhances the ability of the Ag electrode to extract photogenerated electrons and suppress bimolecular recombination in the device [30]. Figure 5(c) graphs V_{oc} as a function of P_{light}, which helps us derive the relationship between V_{oc} and P_{light} using the following equation [41]

$$V_{oc} = \frac{nkT}{q}\ln\left(\frac{J_{ph}}{J_0}+1\right) \quad (1)$$

where n denotes the ideal factor, k is the Boltzmann constant, T denotes the temperature, q is the elementary charge, J_{ph} is the photocurrent and J_0 denotes the dark-saturated photocurrent. Because J_{ph} varies linearly with P_{light} and $\frac{J_{ph}}{J_0} \gg 1$, Eq. (1) can be written as follows

$$V_{oc} = \frac{nkT}{q}\ln P + C(T) \quad (2)$$

where $C(T)$ is a temperature factor independent of P_{light}.

As n approaches 1, trap-assisted recombination diminishes, whereas its greater deviation from 1 signifies an increasing occurrence of trap-assisted recombination [41]. For the BCP-based device, n was 1.41, whereas it decreases to 1.13 for the BCDS-based device. This reduction in n indicates an effective suppression of trap-assisted recombination. This improvement stems from the comprehensive coverage of the perovskite film by the PCBM/BCDS layer (Fig. S13 in the ESM). Furthermore, the penetration of BCDS solution through the PCBM layer enables select BCDS molecules to infiltrate the PCBM/perovskite interface. The sulfonic acid groups on BCDS molecules effectively bond with the undercoordinated Pb^{2+} on the perovskite surface, resulting in a passivation effect that

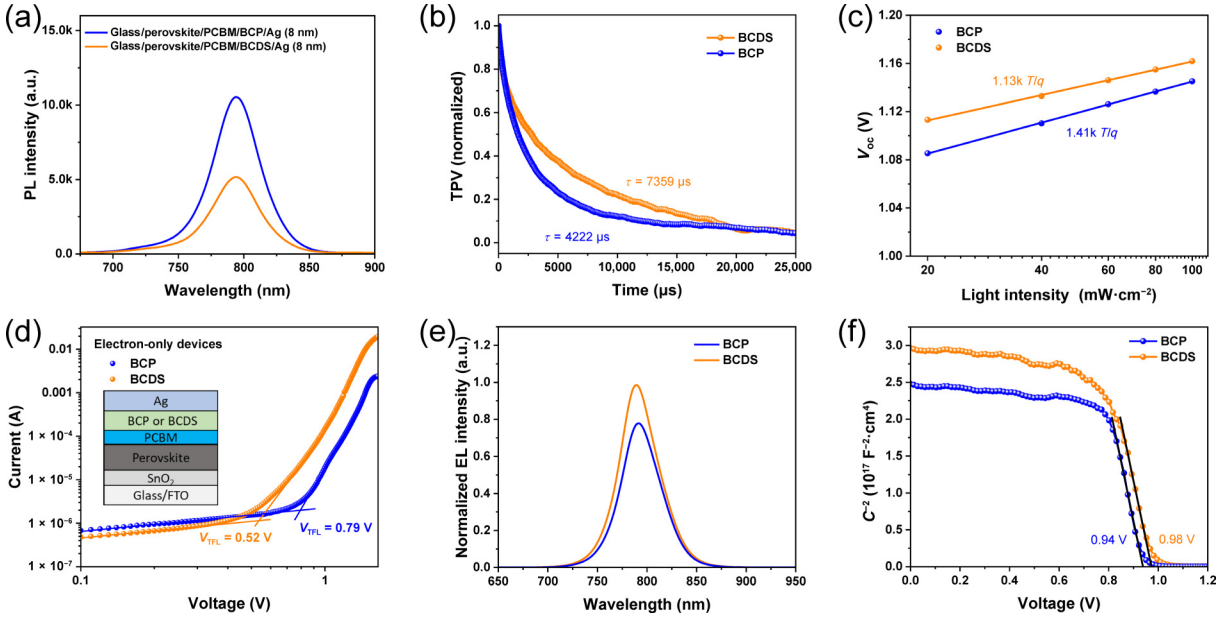

Figure 5 (a) PL spectra of the half devices based on different buffer layers. (b) TPV versus time and (c) V_{oc} versus light intensity curves of the devices based on different buffer layers. (d) SCLC curves of the electron-only devices based on different buffer layers. (e) EL spectra and (f) Mott–Schottky plots obtained at 100 Hz for the devices based on different buffer layers.

enhances overall performance [42]. The trap state densities (N_{trap}) of the devices were further assessed using space-charge-limited current (SCLC) measurements. Electron-only devices with structure of FTO/SnO_2/perovskite/PCBM/BCP (or BCDS)/Ag were fabricated and characterized by *J*–*V* measurements in the dark, as illustrated in Fig. 5(d). The trap-filled limit voltage (V_{TFL}) of the BCP-based device was 0.79 V, which decreased to 0.52 V for the BCDS-based device. The N_{trap} was calculated using the following equation [43]

$$N_{trap} = \frac{2\varepsilon_0\varepsilon_r}{eL^2} V_{TFL} \quad (3)$$

where ε_0 denotes the vacuum permittivity, ε_r is the relative dielectric constant of the perovskite film, e is the elementary charge and L denotes the perovskite layer thickness, which was of approximately 650 nm. The calculated N_{trap} values of the BCP-based and BCDS-based devices were 5.96×10^{15} and 3.92×10^{15} cm^{-3}, respectively. This reduction is inferred to have enhanced the charge extraction and charge transfer efficiencies.

Electroluminescence (EL) measurements were performed to investigate interface recombination in the devices. As depicted in Fig. 5(e), the BCDS-device exhibited enhanced EL intensity, indicating a significant suppression of interface recombination [44]. Capacitance–voltage (*C*–*V*) measurements were conducted on the PSCs incorporating the BCP and BCDS buffer layers and the obtained results are plotted in Fig. 5(f). The built-in voltage (V_{bi}) of the devices can be extracted using the Mott–Schottky equation [45]

$$\frac{1}{C^2} = \frac{2(V_{bi} - V)}{A^2 e\varepsilon_0\varepsilon_r N} \quad (4)$$

where C denotes the capacitance in the space charge region, V is the applied voltage, A is the area of the device and N denotes the carrier concentration. The V_{bi} value can be determined by identifying the point of intersection between the Mott–Schottky curves and the *x*-axis. The device utilizing a BCDS buffer layer exhibits a V_{bi} of 0.98 V, surpassing that of the BCP device (0.94 V). This increased V_{bi} facilitates charge transfer and extraction, potentially mitigating the recombination losses in the devices [46]. These findings are consistent with the observed higher V_{oc} values in the BCDS devices during *J*–*V* testing (Figs. 1(d) and 1(e)). The electrical impedance spectroscopy (EIS) results, as depicted in Fig. S14 and Table S6 in the ESM, further corroborate this by revealing a decrease in series resistance (R_s) and an increase in recombination resistance (R_{rec}) for the BCDS-based device compared to the BCP-based device.

4 Conclusion

In conclusion, we successfully utilized BCDS as a cathode buffer layer in inverted PSCs, superseding conventional BCP-based PSCs. Notably, BCDS-based PSCs exhibited superior conductivity and energy-level alignment compared with their BCP-based counterparts, leading to improved performance. In particular, the sulfonate groups on the BCDS molecules enhanced their interaction with the Ag electrode, thereby augmenting the charge extraction efficiency at the cathode interface of the inverted PSCs. This enhancement translates into a remarkable PCE of 25.06%, which significantly surpasses that of the control device that utilizes BCP as the buffer layer. Furthermore, the uniform film formation of BCDS on PCBM enhanced the device stability, retaining 96% of its initial efficiency after storage in dry air for over 2000 h. These findings demonstrate the significant potential of coordination group modification for enhancing the charge extraction capability at the cathode interface, offering a promising new direction for buffer layer development and performance optimization of PSCs.

Electronic Supplementary Material: Supplementary material (Figs. S1–S14 and Tables S1–S6 including the cross-sectional SEM image, *J*–*V* characteristics, statistical distribution, stabilized power output test, environmental stability, tauc plots, TRPL, dark *J*–*V* characterization, TPC, light intensity test, SEM images, photovoltaic parameters, detailed data of the energy level and fitting parameters of the TRPL results) is available in the online version of this article at https://doi.org/10.26599/NR.2025.94907075.

Data availability

All data needed to support the conclusions in the paper are presented in the manuscript and the Electronic Supplementary Material. Additional data related to this paper may be requested from the corresponding author upon request.

Acknowledgements

This work was supported financially by the National Key R&D Program of China (No. 2023YFE0111500) and the National Natural Science Foundation of China (Nos. 62204222, 52103237, 52321006, T2394480 and T2394484).

Declaration of competing interest

All the contributing authors report no conflict of interests in this work.

Author contribution statement

Z. Q. L.: Investigation, data curation, writing – original draft; Z. Q. R.: Validation, formal analysis, funding acquisition; Z. Y. W.: Conceptualization, formal analysis, data curation, writing – review & editing, supervision, funding acquisition; N. Y.: Investigation, methodology; L. L.: Investigation; B. Z.: Investigation; Y. L. S.: Supervision, writing – review & editing, funding acquisition. All the authors have approved the final manuscript.

Use of AI statement

None.

References

[1] Chen, B.; Rudd, P. N.; Yang, S.; Yuan, Y. B.; Huang, J. S. Imperfections and their passivation in halide perovskite solar cells. *Chem. Soc. Rev.* **2019**, *48*, 3842–3867.

[2] Jin, Y. B.; Feng, H. P.; Fang, Z.; Yang, L.; Liu, K. K.; Deng, B. R.; Chen, J. F.; Chen, X. L.; Zhong, Y. W.; Yang, J. X. et al. Stabilizing semi-transparent perovskite solar cells with a polymer composite hole transport layer. *Nano Res.* **2024**, *17*, 1500–1507.

[3] Zhou, J. J.; Tan, L. G.; Liu, Y.; Li, H.; Liu, X. P.; Li, M. H.; Wang, S. Y.; Zhang, Y.; Jiang, C. F.; Hua, R. M. et al. Highly efficient and stable perovskite solar cells via a multifunctional hole transporting material. *Joule* **2024**, *8*, 1691–1706.

[4] Chen, H.; Liu, C.; Xu, J.; Maxwell, A.; Zhou, W.; Yang, Y.; Zhou, Q. L.; Bati, A. S. R.; Wan, H. Y.; Wang, Z. W. et al. Improved charge extraction in inverted perovskite solar cells with dual-site-binding ligands. *Science* **2024**, *384*, 189–193.

[5] Chin, X. Y.; Turkay, D.; Steele, J. A.; Tabean, S.; Eswara, S.; Mensi, M.; Fiala, P.; Wolff, C. M.; Paracchino, A.; Artuk, K. et al. Interface passivation for 31.25%-efficient perovskite/silicon tandem solar cells. *Science* **2023**, *381*, 59–63.

[6] Kim, D. H.; Muzzillo, C. P.; Tong, J. H.; Palmstrom, A. F.; Larson, B. W.; Choi, C.; Harvey, S. P.; Glynn, S.; Whitaker, J. B.; Zhang, F. et al. Bimolecular additives improve wide-band-gap perovskites for efficient tandem solar cells with CIGS. *Joule* **2019**, *3*, 1734–1745.

[7] Ye, S. Y.; Rao, H. X.; Zhao, Z. R.; Zhang, L. J.; Bao, H. L.; Sun, W. H.; Li, Y. L.; Gu, F. D.; Wang, J. Q.; Liu, Z. W. et al. A breakthrough efficiency of 19.9% obtained in inverted perovskite solar cells by using an efficient trap state passivator Cu(thiourea)I. *J. Am. Chem. Soc.* **2017**, *139*, 7504–7512.

[8] Wang, X.; Rakstys, K.; Jack, K.; Jin, H.; Lai, J.; Li, H.; Ranasinghe, C. S. K.; Saghaei, J.; Zhang, G. R.; Burn, P. L. et al. Engineering fluorinated-cation containing inverted perovskite solar cells with an efficiency of > 21% and improved stability towards humidity. *Nat. Commun.* **2021**, *12*, 52.

[9] Jiang, Q.; Tong, J. H.; Xian, Y. M.; Kerner, R. A.; Dunfield, S. P.; Xiao, C. X.; Scheidt, R. A.; Kuciauskas, D.; Wang, X. M.; Hautzinger, M. P. et al. Surface reaction for efficient and stable inverted perovskite solar cells. *Nature* **2022**, *611*, 278–283.

[10] Sun, A. X.; Tian, C. C.; Zhuang, R. S.; Chen, C.; Zheng, Y. T.; Wu, X. Y.; Tang, C.; Liu, Y.; Li, Z. H.; Ouyang, B. L. et al. High open-circuit voltage (1.197 V) in large-area (1 cm^2) inverted perovskite solar cell via interface planarization and highly polar self-assembled monolayer. *Adv. Energy Mater.* **2024**, *14*, 2303941.

[11] Tang, H. C.; Shen, Z. C.; Shen, Y. Z.; Yan, G.; Wang, Y. B.; Han, Q. F.; Han, L. Y. Reinforcing self-assembly of hole transport molecules for stable inverted perovskite solar cells. *Science* **2024**, *383*, 1236–1240.

[12] Shao, Y. C.; Xiao, Z. G.; Bi, C.; Yuan, Y. B.; Huang, J. S. Origin and elimination of photocurrent hysteresis by fullerene passivation in $CH_3NH_3PbI_3$ planar heterojunction solar cells. *Nat. Commun.* **2014**, *5*, 5784.

[13] Liu, K. K.; Tian, C. B.; Liang, Y. M.; Luo, Y. J.; Xie, L. Q.; Wei, Z. H. Progress toward understanding the fullerene-related chemical interactions in perovskite solar cells. *Nano Res.* **2022**, *15*, 7139–7153.

[14] Li, H.; Xie, G. S.; Fang, J.; Wang, X.; Li, S. B.; Lin, D. X.; Wang, D. Z.; Huang, N. S.; Peng, H. C.; Qiu, L. B. Holistic dielectric and buffer interfacial layers enable high-efficiency perovskite solar cells and modules. *Nano Energy* **2024**, *124*, 109507.

[15] Chen, C. L.; Zhang, S. S.; Wu, S. H.; Zhang, W. J.; Zhu, H. M.; Xiong, Z. Z.; Zhang, Y. J.; Chen, W. Effect of BCP buffer layer on eliminating charge accumulation for high performance of inverted perovskite solar cells. *RSC Adv.* **2017**, *7*, 35819–35826.

[16] Lee, K.; Ryu, J.; Yu, H.; Yun, J.; Lee, J.; Jang, J. Enhanced efficiency and air-stability of NiO_X-based perovskite solar cells via PCBM electron transport layer modification with Triton X-100. *Nanoscale* **2017**, *9*, 16249–16255.

[17] Li, M.; Zhao, C.; Wang, Z. K.; Zhang, C. C.; Lee, H. K. H.; Pockett, A.; Barbé, J.; Tsoi, W. C.; Yang, Y. G.; Carnie, M. J. et al. Interface modification by ionic liquid: A promising candidate for indoor light harvesting and stability improvement of planar perovskite solar cells. *Adv. Energy Mater.* **2018**, *8*, 1801509.

[18] Cui, C. H.; Li, Y. W.; Li, Y. F. Fullerene derivatives for the applications as acceptor and cathode buffer layer materials for organic and perovskite solar cells. *Adv. Energy Mater.* **2017**, *7*, 1601251.

[19] Chen, P.; Xiao, Y.; Hu, J. T.; Li, S. D.; Luo, D. Y.; Su, R.; Caprioglio, P.; Kaienburg, P.; Jia, X. H.; Chen, N. et al. Multifunctional ytterbium oxide buffer for perovskite solar cells. *Nature* **2024**, *625*, 516–522.

[20] Da, P. M.; Zheng, G. F. Tailoring interface of lead-halide perovskite solar cells. *Nano Res.* **2017**, *10*, 1471–1497.

[21] Chen, Y. H.; Chen, T.; Dai, L. M. Layer-by-layer growth of $CH_3NH_3PbI_{3-x}Cl_x$ for highly efficient planar heterojunction perovskite solar cells. *Adv. Mater.* **2015**, *27*, 1053–1059.

[22] Jiang, Z. Y.; Pan, M.; Ren, F. M.; Chen, R.; Sun, Z. X.; Yang, Z. C.; Liu, Z. H.; Chen, W. Boosting stability of inverted perovskite solar cells with magnetron-sputtered molybdenum rear electrodes. *Rare Met.* **2023**, *42*, 3741–3754.

[23] Menzel, D.; Al-Ashouri, A.; Tejada, A.; Levine, I.; Guerra, J. A.; Rech, B.; Albrecht, S.; Korte, L. Field effect passivation in perovskite solar cells by a LiF interlayer. *Adv. Energy Mater.* **2022**, *12*, 2201109.

[24] Huang, Y. L.; Liu, T. H.; Wang, B. Z.; Li, J. L.; Li, D. Y.; Wang, G. L.; Lian, Q.; Amini, A.; Chen, S.; Cheng, C. et al. Antisolvent engineering to optimize grain crystallinity and hole-blocking capability of perovskite films for high-performance photovoltaics. *Adv. Mater.* **2021**, *33*, 2102816.

[25] Chang, C. Y.; Lee, K. T.; Huang, W. K.; Siao, H. Y.; Chang, Y. C. High-performance, air-stable, low-temperature processed semitransparent perovskite solar cells enabled by atomic layer deposition. *Chem. Mater.* **2015**, *27*, 5122–5130.

[26] Kim, I. S.; Cao, D. H.; Buchholz, D. B.; Emery, J. D.; Farha, O. K.; Hupp, J. T.; Kanatzidis, M. G.; Martinson, A. B. F. Liquid water- and heat-resistant hybrid perovskite photovoltaics via an inverted ALD oxide electron extraction layer design. *Nano Lett.* **2016**, *16*, 7786–7790.

[27] Yu, S. Q.; Xiong, Z.; Zhou, H. T.; Zhang, Q.; Wang, Z. H.; Ma, F.; Qu, Z. H.; Zhao, Y.; Chu, X. B.; Zhang, X. W. et al. Homogenized NiO_x nanoparticles for improved hole transport in inverted perovskite solar cells. *Science* **2023**, *382*, 1399–1404.

[28] Liu, N. H.; Xiong, J.; Wang, G.; He, Z.; Dai, J. Q.; Zhang, Y. S.; Huang, Y.; Zhang, Z. L.; Wang, D. J.; Li, S. et al. Overcoming the PCBM/Ag interface issues in inverted perovskite solar cells by rhodamine-functionalized dodecahydro-*closo*-dodecaborate derivate interlayer. *Adv. Funct. Mater.* **2023**, *33*, 2300396.

[29] Azmi, R.; Ugur, E.; Seitkhan, A.; Aljamaan, F.; Subbiah, A. S.; Liu, J.; Harrison, G. T.; Nugraha, M. I.; Eswaran, M. K.; Babics, M. et al. Damp heat-stable perovskite solar cells with tailored-dimensionality 2D/3D heterojunctions. *Science* **2022**, *376*, 73–77.

[30] Henderson, C.; Luke, J.; Bicalho, I. S.; Correa, L.; Yang, E. J.; Rimmele, M.; Demetriou, H.; Chin, Y. C.; Lan, T. H.; Heutz, S. et al. Charge transfer complex formation between organic interlayers drives light-soaking in large area perovskite solar cells. *Energy Environ. Sci.* **2023**, *16*, 5891–5903.

[31] Yang, J. B.; Cao, Q.; Wang, T.; Yang, B. W.; Pu, X. Y.; Zhang, Y. X.; Chen, H.; Tojiboyev, I.; Li, Y. K.; Etgar, L. et al. Inhibiting metal-inward diffusion-induced degradation through strong chemical coordination toward stable and efficient inverted perovskite solar cells. *Energy Environ. Sci.* **2022**, *15*, 2154–2163.

[32] Cheng, F. W.; Zhan, S. Q.; Cai, Y. T.; Cao, F.; Dai, X. F.; Xu, R. C.; Yin, J.; Li, J.; Zheng, N. F.; Wu, B. H. Interfacial property tuning enables copper electrodes in high-performance n–i–p perovskite solar cells. *J. Am. Chem. Soc.* **2023**, *145*, 20081–20087.

[33] Shibayama, N.; Kanda, H.; Kim, T. W.; Segawa, H.; Ito, S. Design of BCP buffer layer for inverted perovskite solar cells using ideal factor. *APL Mater.* **2019**, *7*, 031117.

[34] Jiang, Q.; Song, Z. N.; Bramante, R. C.; Ndione, P. F.; Tirawat, R.; Berry, J. J.; Yan, Y. F.; Zhu, K. Highly efficient bifacial single-junction perovskite solar cells. *Joule* **2023**, *7*, 1543–1555.

[35] Gaikar, V. G.; Padalkar, K. V.; Aswal, V. K. Characterization of mixed micelles of structural isomers of sodium butyl benzene sulfonate and sodium dodecyl sulfate by SANS, FTIR spectroscopy and NMR spectroscopy. *J. Mol. Liq.* **2008**, *138*, 155–167.

[36] Kazachenko, A. S.; Akman, F.; Abdelmoulahi, H.; Issaoui, N.; Malyar, Y. N.; Al-Dossary, O.; Wojcik, M. J. Intermolecular hydrogen bonds interactions in water clusters of ammonium

sulfamate: FTIR, X-ray diffraction, AIM, DFT, RDG, ELF, NBO analysis. *J. Mol. Liq.* **2021**, *342*, 117475.

[37] Cao, Y.; Feng, J. S.; Wang, M. Z.; Yan, N.; Lou, J. J.; Feng, X. L.; Xiao, F. W.; Liu, Y. C.; Qi, D. Y.; Yuan, Y. et al. Interface modification by ammonium sulfamate for high-efficiency and stable perovskite solar cells. *Adv. Energy Mater.* **2023**, *13*, 2302103.

[38] Nasef, M. M.; Saidi, H. Surface studies of radiation grafted sulfonic acid membranes: XPS and SEM analysis. *Appl. Surf. Sci.* **2006**, *252*, 3073–3084.

[39] Chang, C. Y.; Chang, Y. C.; Huang, W. K.; Liao, W. C.; Wang, H.; Yeh, C.; Tsai, B. C.; Huang, Y. C.; Tsao, C. S. Achieving high efficiency and improved stability in large-area ITO-free perovskite solar cells with thiol-functionalized self-assembled monolayers. *J. Mater. Chem. A* **2016**, *4*, 7903–7913.

[40] Yang, T. H.; Gao, L. L.; Lu, J.; Ma, C.; Du, Y. C.; Wang, P. J.; Ding, Z. C.; Wang, S. Q.; Xu, P.; Liu, D. L. et al. One-stone-for-two-birds strategy to attain beyond 25% perovskite solar cells. *Nat. Commun.* **2023**, *14*, 839.

[41] Elumalai, N. K.; Uddin, A. Open circuit voltage of organic solar cells: An in-depth review. *Energy Environ. Sci.* **2016**, *9*, 391–410.

[42] Chiang, S. E.; Chandel, A.; Thakur, D.; Chen, Y. T.; Lin, P. C.; Wu, J. R.; Cai, K. B.; Kassou, S.; Yeh, J. M.; Yuan, C. T. et al. On the role of solution-processed bathocuproine in high-efficiency inverted perovskite solar cells. *Solar Energy* **2021**, *218*, 142–149.

[43] Gao, Y.; Xu, W. Z.; He, F.; Nie, P. B.; Yang, Q. D.; Si, Z. C.; Meng, H.; Wei, G. D. Carbon nanodots enhanced performance of $Cs_{0.15}FA_{0.85}PbI_3$ perovskite solar cells. *Nano Res.* **2021**, *14*, 2294–2300.

[44] Sun, C.; Yang, P. P.; Nan, Z. A.; Tian, C. B.; Cai, Y. T.; Chen, J. F.; Qi, F. F.; Tian, H. R.; Xie, L. Q.; Meng, L. Y. et al. Well-defined fullerene bisadducts enable high-performance tin-based perovskite solar cells. *Adv. Mater.* **2023**, *35*, 2205603.

[45] Sui, Y. J.; Zhou, W. C.; Khan, D.; Wang, S. L.; Zhang, T.; Yu, G. P.; Huang, Y. M.; Yang, X. Q.; Chang, K.; He, Y. C. et al. Understanding the role of crown ether functionalization in inverted perovskite solar cells. *ACS Energy Lett.* **2024**, *9*, 1518–1526.

[46] Tuo, B. Y.; Wang, Z. Y.; Ren, Z. Q.; Zhang, H. W.; Lu, X. Q.; Zhang, Y. Q.; Zang, S. Q.; Song, Y. L. A novel radical-reaction interruption strategy for enhancing the light stability of perovskite solar cells. *Energy Environ. Sci.* **2024**, *17*, 2945–2955.